Turbulent convection of suspended sediments due to flow reversal

Yeon S. Chang[1] and Alberto Scotti[2]

Received 22 August 2005; revised 7 March 2006; accepted 17 March 2006; published 1 July 2006.

[1] We investigate the ejection of sediments from the near-bed region of a pulsating boundary layer over a flat bottom. The boundary layer flows were generated using Large Eddy Simulation (LES) while the motion of individual particles was calculated using a modified version of the Maxey and Riley equation. The suspension rate of near-bed sediment particles sharply increases during decelerating flow phase and peaks near the time of local flow reversals. This suspension pattern of sediments was closely related to the near-bed turbulent vortex structures which evolve during a wave cycle. During period of maximum flow rate, the horizontally aligned vortex cores retarded settling of sediment particles. As the flow decelerates, vertically organized vortices induce an upward flux of particles. Vertical velocity fluctuations are strongest at the time of flow reversal, leading to maximum sediment suspension at this time. These results are shown to be incompatible with simple eddy-diffusivity models for sediment transport.

Citation: Chang, Y. S., and A. Scotti (2006), Turbulent convection of suspended sediments due to flow reversal, *J. Geophys. Res.*, *111*, C07001, doi:10.1029/2005JC003240.

1. Introduction

[2] The mechanism responsible for the uplift of sediments from the near-wall region of an unsteady (oscillating or pulsating) boundary layer into the outer flow is still debated. While turbulent diffusion has been largely accepted as the major mixing mechanism in modeling the sediment concentration profiles [*Freds and Deigaard*, 1992; *Andersen*, 1999; *Holmedal et al.*, 2004], convective flux has also been indicated as a viable candidate [*Nielsen*, 1992; *Li and Davis*, 1996]. In diffusion-type models the upward flux of suspended sediments is balanced by the sediment settling and its magnitude is controlled by an eddy diffusivity, commonly set equal to an eddy viscosity. In this framework, suspended sediment profiles would be incorrect unless the mixing due to turbulent fluctuations is precisely accounted by the eddy viscosity [*Chang and Hanes*, 2004; *Chang and Scotti*, 2004]. Models of this type usually fail to produce a second peak of near-bed sediment concentration at flow reversals although observations suggest otherwise [*Li and Davis*, 1996; *O'Donoghue and Wright*, 2004] and poorly supports the sediment entrainment at times of low shear stresses during a wave cycle. Turbulent convection is another sediment mixing process that usually occurs by traveling vortices over rippled beds, and it is distinguished from diffusion by larger mixing scales [*Nielsen*, 1992]. Although the importance of sediment convection has been widely recognized, it is still not generally accepted in modeling sediment suspension, and only a few conceptual models have been available [*Lee and Hanes*, 1996].

[3] These sediment suspension processes are also highly correlated with boundary conditions because this determines the amount of sediments to be suspended from the seabed and also determines the time of maximum/minimum sediment entrainment according to wave phases. Commonly, two approaches are used in applying boundary conditions: reference concentrations and pick up functions. In the reference concentration approach, the concentration of sediments is specified at a reference level usually specified either as twice the grain diameter, $z_0 = 2 * D_{50}$ [*Einstein*, 1950; *Eungelund and Fredsoe*, 1976] or at a much higher level [*van Rijn*, 1984b; *Smith and McLean*, 1977; *Garcia and Parker*, 1991] depending on the characteristics of the saltating motion. There have been various expressions for the reference concentration based upon physical and experimental considerations [*Eungelund and Fredsoe*, 1976; *van Rijn*, 1984b; *Smith and McLean*, 1977; *Zyserman and Fredsoe*, 1994]. In essence, the concentration is set proportional to the Shields parameter. This approach supports diffusive sediment mixing, expected to be strongest at maximum flow rates owing to both high shear in the flow as well as high sediment concentrations. Sediment mixing by convection is, however, poorly supported by reference concentration, especially when the bottom shear is minimal.

[4] In the pick-up function approach, the instantaneous sediment flux at bed level is provided under the assumption that entrainment and deposition are independent processes. This approach strongly supports the upward convective flux of sediment particles even at low shear stresses because it does not require balancing with the downward motions of settling sediments. On the basis of the experimental expression for a pick-up function in uniform flows [*van Rijn*, 1984a,

[1]Meteorology and Physical Oceanography, Rosenstiel School of Marine and Atmospheric Science, University of Miami, Miami, Florida, USA.
[2]Department of Marine Sciences, University of North Carolina, Chapel Hill, North Carolina, USA.

0148-0227/06/2005JC003240

1986], Nielsen modified this methodology to be applied in unsteady flows allowing correspondence between maximum entrainment rate and the time of near-bed flow reversal [*Nielsen*, 1992].

[5] For the fluid phase, Reynolds-Averaged Navier-Stokes (RANS) equations are often employed [*Saffman*, 1970; *Launder and Sharma*, 1974; *Tjerry*, 1995; *Wilcox*, 1998]. RANS models are the preferred tools for coastal engineering applications due to their robustness and relatively small computational cost. However, since fluctuations at all scales need to be modeled, the models are sensitive to large-scale driving conditions. For example, recent evidence suggests that commonly used RANS models misrepresent key turbulent quantities in unsteady boundary layers [*Chang and Scotti*, 2004]. At the opposite end of the modeling spectrum, Direct Numerical Simulation (DNS) has been successfully employed in many studies of oscillating boundary layers [*Vittori and Verzicco*, 1998; *Scandura et al.*, 2000; *Moin and Manesh*, 1998]. DNS simulations are however severely limited by grid size and time step requirements. For this reason, DNS is still confined to relatively low Reynolds number flows. Large Eddy Simulation (LES) steers a middle course between DNS and RANS. In LES the large-scale eddies that are considered to be important in energy transfer are resolved, and the smallest "subgrid-scale"(SGS) eddies are modeled [*Moin and Kim*, 1982; *Rogallo and Moin*, 1984]. Hence the LES approach lies between the extremes of DNS in which all fluctuations are resolved, and RANS in which only mean values are calculated and all fluctuations are modeled. For this reason LES results are usually less sensitive to modeling errors than RANS method.

[6] In modeling sediment motions, the sediment conservation equation has been commonly coupled with RANS [*Andersen*, 1999; *Holmedal et al.*, 2004; *Li and Davis*, 1996] or LES [*Zedler and Street*, 2001] to estimate the volume concentration of sediments. Although this calculation of concentration is efficient for practical purposes, it does not allow the precise description of the instantaneous response of sediment particles to ambient flows. To address these issues, LES or DNS have been coupled to an equation for the particulate phase [*Pedinotti et al.*, 1992; *Wang and Squires*, 1996; *Armenio et al.*, 1999]. Recently, the influence of instantaneous flow turbulence on sediment transport has been investigated using these high-accuracy turbulence schemes. *Chang and Scotti* [2003] found that the streamwise coherent vortices captured sediment grains and transported them over a ripple crest in a steady flow by coupling a sediment particulate equation into LES. *Vittori* [2003] numerically investigated the interactions of turbulent vortices with sediments in a pure oscillating flow over a flat bed by employing a simple equation for sediment motions. This investigation demonstrated long turbulent vortex streaks were broken up generating small vortices that increased the mixing effects during decelerating flows, resulting in maximum pick up rate during this flow phase. Although her study greatly enhanced the understanding of suspension events in relation to the distribution of turbulent structures, the role of these structures on sediment dispersion in terms of the mixing process by diffusion or convection requires verification, and more importantly, the questions of why the sediment entrainment is maximum at that time and the role of flow reversals on this remain unanswered.

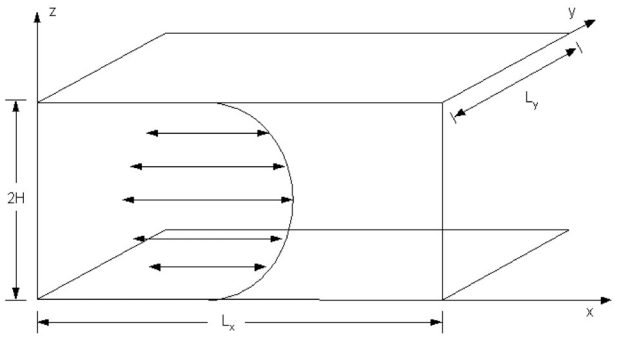

Figure 1. Schematic of the computational domain.

[7] By investigating the development of turbulent vortex structures and their influence on the sediment motions, we study sediment mixing due to convective processes. We do this with LES coupled with a modified Maxey and Riley equation [*Maxey and Riley*, 1983; *Wiberg and Smith*, 1985; *Drake and Calantoni*, 2001]. The approach is similar to that of *Vittori* [2003], only here we use a more complete equation for the transport of particles. Unsteady flow conditions were driven with parameters as close as possible to the ones found in the coastal environment. To isolate the effect of turbulent structures from large-scale vortical motion, we considered a flat, hydrodynamically smooth surface.

2. Problem Formulation

[8] We assume that the concentration of sediments at any time is too low to affect the dynamics of the fluid. Thus the equations for the fluid part can be solved independently from the particulate phase (one-way coupling).

2.1. Fluid Equations

[9] The governing equations employed in the present study for the fluid phase are the filtered Navier-Stokes equations,

$$\frac{\partial \tilde{u}_i}{\partial t} + \frac{\partial}{\partial x_j}\left(\tilde{u}_i \tilde{u}_j\right) = -\frac{\partial \tilde{P}}{\partial x_i} + \nu \frac{\partial^2 \tilde{u}_i}{\partial x_j \partial x_j} - \frac{\partial \tau_{ij}}{\partial x_j} \tag{1}$$

$$\frac{\partial \tilde{u}_i}{\partial x_i} = 0, \tag{2}$$

where the subgrid scale stress is

$$\tau_{ij} = \left(\widetilde{u_i u_j} - \tilde{u}_i \tilde{u}_j\right). \tag{3}$$

[10] In the above equations, a tilde is used to indicate filtered variables. The computational domain is a rectangular channel with height = 0.2 m, and width = 0.6 m and 0.2 m, respectively (Figure 1) and the viscosity $\nu = 10^{-6}$ m^2/s. The use of close-channel geometry is considered standard in turbulence studies, and was chosen so that comparison with laboratory experiments in closed channel be possible. Moreover, since the emphasis is on the behavior in the near-wall region, the nature of the upper boundary conditions has a minor effect. A posteriori comparison with the experiments of *O'Donoghue and Wright* [2004] (see below) further supports

this choice. The subgrid-scale stress in equation (3) is modeled using the dynamic eddy viscosity model [*Germano et al.*, 1991; *Lilly*, 1992]. The flow is forced by an external pressure gradient that is the sum of a steady and an oscillating part,

$$P_f(x,t) = [\alpha + \beta\cos(\omega t)]x. \tag{4}$$

The total pressure, $P(x, y, z, t)$, is the sum of the forcing pressure, $P_f(x, t)$, and the mechanical pressure, $p(x, y, z, t)$, the latter necessary to satisfy the zero divergence condition of the flow. Equations (1)–(3) are solved using an Adams-Bashforth fractional-step method. Both advective and diffusive terms are treated explicitly. All spatial derivatives are approximated by second-order central differences on a staggered grid [*Balaras*, 1995]. The boundary conditions are periodic in x and y, and no-slip at the lower and upper boundary. The grid spacing is uniform in the spanwise and streamwise direction. In the vertical direction, a hypertangential grid generator is employed to create dense grid spacing near the lower wall. Periodic boundary conditions are commonly employed along homogeneous directions, provided that the extent of the computational domain is sufficiently large to capture the size of the largest streamwise eddies.

2.2. Sediment Particle Motion

[11] We use the equation derived by *Wiberg and Smith* [1985] to describe the force balance acting on sediment particles in water. Buoyancy, pressure gradient of ambient flow, added mass, drag, and lift forces are included in the force balance that reads

$$\begin{aligned}\frac{\rho_p}{\rho}\frac{d\vec{V}_p}{dt} = &-\left(\frac{\rho_p}{\rho}-1\right)Vg\vec{n} + V\frac{D\vec{u}_f}{Dt} + C_m V\left(\frac{D\vec{u}_f}{Dt} - \frac{d\vec{V}_p}{dt}\right)\\ &+\frac{1}{2}C_D A|\vec{u}_f - \vec{V}_p|(\vec{u}_f - \vec{V}_p)\\ &+\frac{1}{2}C_L A\left(|\vec{u}_f - \vec{V}_p|^2_{top} - |\vec{u}_f - \vec{V}_p|^2_{bot}\right)\vec{n},\end{aligned} \tag{5}$$

where V_p is sediment particle velocity vector, u_f is fluid velocity interpolated at the particle position, ρ_p and ρ are the density of particle and fluid, respectively, V and A are the volume and cross sectional area of the particle, C_m is the coefficient of added mass, C_D and C_L are drag and lift coefficients, $\vec{n}$ is a vector of magnitude one pointing upward. The subscripts "top" and "bot" mean that the relative velocities are calculated at the top and bottom of the sediment particle and the derivative D/Dt denote the time derivative following a parcel of fluid such that $\frac{D}{Dt} = \frac{\partial}{\partial t} + u_{fj}\frac{\partial}{\partial x_j}$. In the above equation, the drag force is replaced by the Stokes drag, $6\pi r\mu(\vec{u}_f - \vec{V}_p)$, when the particle Reynolds number $Re_p = D|\vec{u}_f - \vec{V}_p|/\nu$ is less than 1. Here μ is the dynamic viscosity of water and r the radius of the particle. The coefficient of added mass, C_m, is 0.5 for a spherical particle and the lift coefficient, C_L, is set to 0.2. The empirical relation for the drag coefficient $C_D = \frac{24}{Re_p}[1 + 0.15Re_p^{0.687}]$ is used following *Wang and Squires* [1996] to account for finite Re_p effects. The lift force induced by the velocity difference between top and bottom of the particle is usually considered negligible when the size of the particle is small. Inside the viscous sublayer, however, the velocity gradient is large, so we have decided to retain it for completeness. Overall, its effects are small. Other forces, such as the Magnus force due to the particle rotation and the Basset history force that accounts for changes in fluid drag due to changes in the flow structure around the particle are ignored in the present study. In a LES, the velocity field contains only information on the resolved scales, whereas in reality the particles are advected by the actual velocity field that contains fluctuations down to the dissipative scale. *Armenio et al.* [1999] showed that the effect of the unresolved scales is small in the statistical sense. Moreover, in the near-wall turbulent Stokes layer, because of the refinement of the grid (see comments below), the subgrid-scale fluctuations become very small. Following current practice [see, e.g., *Marchioli et al.*, 2006], we ignore this effect. The particle velocities are calculated by integrating equation (5) in time using a semi-implicit method. Since the particle positions at any given time do not in general correspond with the points at which the Eulerian fluid velocity field is known, the velocity field and its derivatives need to be interpolated onto the particle position. The interpolation is carried out by sixth-order Lagrangian polynomials in three directions [*Balachandar and Maxey*, 1989]. Once the particle velocities are computed, the particle displacement can be calculated from

$$\frac{d\vec{X}_p}{dt} = \vec{V}_p, \tag{6}$$

where $\vec{X}_p$ is the position vector of the sediment particle. At the horizontal boundaries, consistent with the periodic boundary conditions for the flow, particles leaving one side are injected at the opposite side. In the vertical direction, the particles are removed if they reach the bottom or the middle of the channel.

2.3. Parameters: Continuum and Particulate Phase

[12] The unsteady flows are generated by specifying α and β in equation (4). The choice of these forcing parameters represents a compromise between achieving the largest possible Reynolds number while keeping the execution time within reasonable bounds. For the steady component $\alpha = 10^{-3}$ m/s^2 gives a friction velocity $u_t = 10^{-2}$ m/s and a Reynolds number based on the friction velocity and height of the channel $Re_t \equiv u_t H/\nu = 1000$. The physical domain is discretized using 98 points in the vertical and 130 points in each horizontal direction. In the vertical, the grid is stretched to accommodate 10 points within the first 10 wall units (1 *w.u.* $\equiv \nu/u_t = 0.1$ mm), while in the horizontal the resolution was 4.7 mm in the streamwise direction and 1.6 mm in the spanwise direction ($\Delta x^+ = \Delta x u_t/\nu = 47$, $\Delta y^+ = \Delta y u_t/\nu = 16$). The typical spanwise scale of streamwise vortices is 100 wall units, while they extend $O(1000)$ wall units in the streamwise direction [*Robinson*, 1991]. Thus the present grid is both large enough to accommodate the structures and fine enough the resolve them appropriately.

[13] For the oscillating part, we set $\beta = 0.3142$ m/s^2 and $T = 8$ s, resulting in a free stream velocity $U_\infty = 0.4$ m/s, a

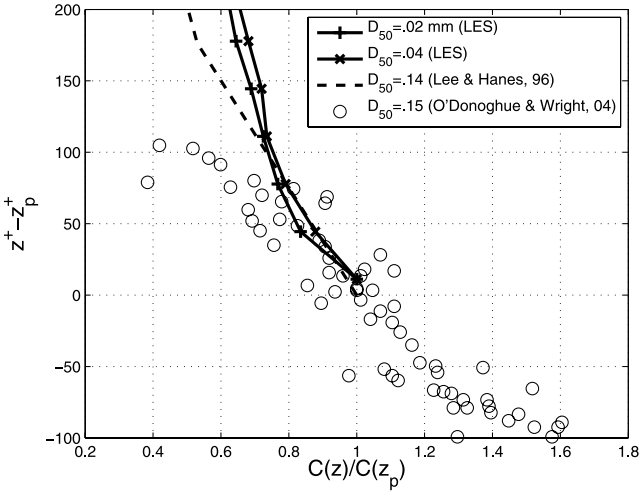

Figure 2. Comparison of sediment concentration profiles with field [*Lee and Hanes*, 1996] and laboratory [*O'Donoghue and Wright*, 2004] data.

realistic value in shallow waters. Oscillating flows over a flat surface can be characterized in terms of a Reynolds number $Re_s = U_\infty l_s/\nu$ based on the thickness of the laminar boundary layer $l_s = \sqrt{2\nu/\omega}$ and the free stream velocity. In the present case, $Re_s = 640$ places the flow in the transitional regime according to *Hino et al.* [1983]. *Scotti and Piomelli* [2001] used LES in a closed channel with the same dynamic SGS model employed here to simulate pulsating flows. Under similar driving conditions, excellent agreement with experimental data was achieved with a ratio $H/l_s = 10$, even though the experiments were performed in taller facilities. This provides further evidence that the present geometry is well suited to capture the physics of the turbulent Stokes layer. Finally, we considered grains of diameter 0.02∼0.04 mm (silt), with a density ratio $S = 2.65$ (quartz).

2.4. Experimental Setup

[14] The solver was run until a statistically steady state (in the sense of phase averages) was reached. At this point, the statistical properties of the solution were checked against standard benchmarks [*Kim et al.*, 1987] and found in good agreement. The field was then used as an initial condition for the flows.

[15] For the particular phase, the assumptions under which equation (5) is derived break down in the immediate vicinity of the lower boundary, at a distance of the order of the diameter of the particles. In this region, one cannot ignore the finite extent of the particles and the complexities due to particle-particle interaction and collision with particles on the bottom [*Bagnold*, 1954]. Ideally, in the viscous sublayer, one should solve the fully coupled laminar problem treating the particles as spheres of finite extent. However, coupling a turbulent channel solver to a 3D coupled laminar solver is computationally too expensive (a 2D simulation of a laminar flow over nearly buoyant particles has been recently published [*Patankar et al.*, 2001], which illustrates well the difficulties involved). Once detached from the bottom, particles can be suspended if, at the zenith of their trajectories, the particles encounter turbulent fluctuations of large enough magnitude, and it is on the latter problem that we focus in this paper. Thus, in the present study, we have decided to ignore the dynamics in the viscous layer, and we have concentrated on the dynamics of the particles outside the viscous layer, where equation (5) is a valid approximation. Thus we followed *Vittori* [2003] and released the particles in the flow at the edge of the viscous sublayer ($z = 0.95$ mm), where vertical turbulent fluctuations are strong enough to suspend particles, and equation (4) applies. For each run, we released 4096 particles and followed them until a pseudo steady state was reached. Particles that hit the bottom or that reached the middle of the channel were removed from the simulation.

3. Results

3.1. Comparison With Experiments

[16] To gauge the validity of our model, we compare the concentration profiles of the pulsating case with profiles obtained in the field [*Lee and Hanes*, 1996] and in the laboratory [*O'Donoghue and Wright*, 2004]. Both data sets were obtained under sheet flow regime under the combined effect of waves and a mean current. The sediment concentrations were calculated from our numerical data by dividing the vertical range into 10 bins from 0 to 0.02 m and by counting the number of particles contained within each segment. Then the vertical profiles were obtained averaging over a wave cycle and over the 5 release time. The particles that have settled to the bottom are not included for counting.

[17] To make the comparison meaningful, it is necessary to introduce appropriate nondimensional units, as the data were collected under different conditions (mean flow velocity, sediment size, etc.). As Figure 2 shows, the agreement is reasonable once we express the distance from the bottom in wall units ($z^+ \equiv u_t\, z/\nu$) and the concentrations referenced to the concentration at the reference level, z_p. The reference level is taken at $z_p = 0.0$ cm for the laboratory data and the numerical data because the flow velocities are zero at this level. For the field data, it is taken at $z = 1.44$ cm, the lowest point were measurements were taken. For the friction velocities we use the values determined experimentally (3.0 cm/s for the laboratory experiments, 3.14 cm/s for the field data). For the numerical data, u^* is set by the value of α employed at 1.0 cm/s. In judging the results, allowance must be made for the fact that the sediments used in the numerical data are smaller than typical field conditions. The value employed here represents a compromise. For a fixed Reynolds number, the probability that a particle released at the edge of the viscous sublayer remains suspended during a cycle decreases with increasing diameter. Numerical constraints limit the maximum Reynolds number as well as the number of particles that can be tracked. Under present conditions, the values chosen for the particle diameter allow a statistically significant number of particles to remain suspended, while still be large enough so as not to behave like passive tracers. Finally, the discrepancy between laboratory and field data and the numerical data at high elevation ($z^+ - z_p^+ \geq 100$) is likely due to differences in boundary conditions and Reynolds number.

3.2. Sediment Motions at Flow Reversal

[18] In order to illustrate the bursting motions of sediments during flow reversal, trajectories of selected sediment

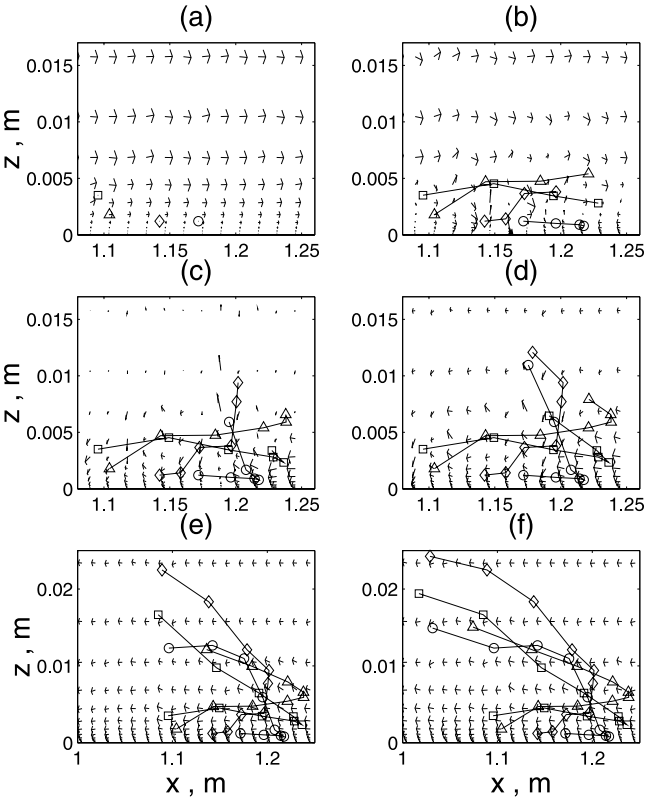

Figure 3. Examples of particle trajectories near the time of flow reversal.

grains are shown in Figure 3 at six times near reversal time. The trajectories and the flow vectors are projected on a $x - z$ plane extending from the bottom to 0.025 m. The range in x direction can be extended beyond the domain size owing to periodic boundary conditions. As shown in Figures 3a and 3b, four particles initially located close to the bed move horizontally without significant changes in their vertical positioning until the flow reverses. at which point the grains gain considerable elevation (Figures 3c and 3d). Once the flow reverses the grains revert to their mainly horizontal trajectories (Figures 3e and 3f).

[19] Further evidence for active sediment ejection due to flow reversal is shown in Figure 4 where the entrainment rate of sediments, $\bar{w}_p$, is estimated by calculating the mean vertical velocities of particles that remain suspended during the entire duration of the experiment. The particles are released at five different times ranging from $t \sim 1$ s to $t \sim 5.5$ s in order to compare the suspension pattern of particles that reach the edge of the viscous sublayer at different times.

[20] The $\bar{w}_p$ of all five groups show a similar pattern with a sharp increase during the decelerating flow phase of the flow($t \sim 5$ s). This result is consistent with *Vittori* [2003], who also observed that the maximum concentration occurred during the decelerating flow phase. Close examination of the phase difference among the five sediment groups reveals phase lags in the maximum values of entrainment rates. As denoted by the thick arrow in Figure 4, the times of maximum rate show a lag which correlates with the release time of the particles. This behavior indicates that the local flow conditions determine the behavior of the particles, since the earlier a particles is released, the higher it gets before the local flow reverses, owing to the lag between inner and outer layer.

[21] It is clear that the sediment bursting motion during local flow reversal cannot be modeled by sediment diffusion alone, because the flow shear is low during this phase. Rather, it is sediment convection as described by *Nielsen* [1992] who recognized the importance of the convective sediment entrainment due to flow reversal. These patterns were also observed by *O'Donoghue and Wright* [2004] where the concentration peaks were found at flow reversal as long as the sediment size remained fine($D_{50} < 0.2$ mm). These peaks were not captured by shear stress based empirical model although good agreement was found for the diffusive sediment flux during the phase of maximum flow.

[22] In order to closely examine the convective nature of sediment ejection during flow reversal, we show the distributions of sediment particles in Figures 5–7. Each figure represents the particle cloud at four times during the first second following release. Three different times are chosen to compare the suspension pattern during maximum flow rate, ($t_0 \sim 3$ s), at the onset of the decelerating phase ($t_0 \sim 4.5$ s), when the flow reverses ($t_0 \sim 5.5$ s). The particle positions are projected on a $y - z$ plane so that the vertical distribution can be compared regardless of their streamwise positions. At maximum flow rate (Figure 5) the particles are found gradually moving upward from their initial elevation, $z_0 = 0.95$ mm. During this time, the particles are uniformly distributed along the y direction. This is one of the characteristics of diffusive motions with no horizontal variations expected without a change in hydrodynamic conditions. Another interesting feature of this flow phase is that the

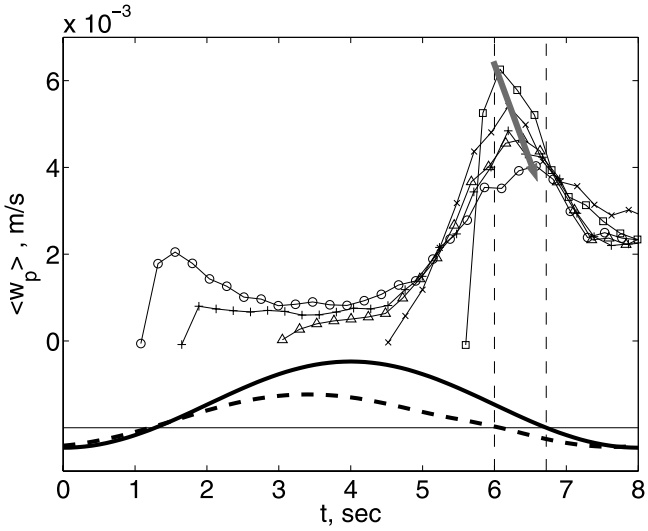

Figure 4. Entrainment rate of (top curves) suspended sediment particles and (bottom curves) mean streamwise flow velocity at $z = 0.1$ m (solid line) and $z = 0.001$ m (dashed line). The sediments are released at five different times over a wave period and marked with different symbols.

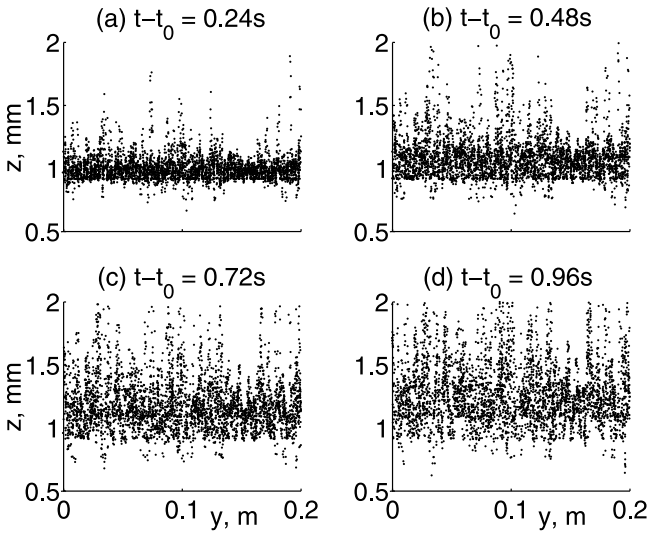

Figure 5. Vertical dispersion of sediment particles on y-z plane at maximum flow rates. Particles are released at z = 0.95 mm and $t_0 \sim$ 3 s. (a) $t - t_0$ = 0.24 s, (b) $t - t_0$ = 0.48 s, (c) $t - t_0$ = 0.72 s, and (d) $t - t_0$ = 0.96 s.

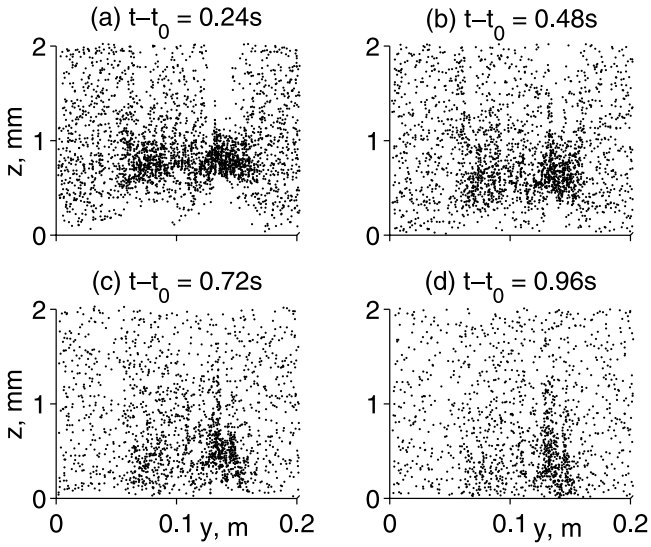

Figure 7. Vertical dispersion of sediment particles on y-z plane around flow reversal. Particles are released at z = 0.95 mm and $t_0 \sim$ 5.5 s. (a) $t - t_0$ = 0.24 s, (b) $t - t_0$ = 0.48 s, (c) $t - t_0$ = 0.72 s, and (d) $t - t_0$ = 0.96 s.

sediment particles are kept from settling (without turbulence, the particle reach the bottom in about 1 s).

[23] Conversely, most of the particles released at the onset of deceleration settle down (Figure 6). The distribution of sediments is not uniform in the y direction This strong concentrated vertical flux becomes even stronger near flow reversal (Figure 7). During this time, with the exception a narrow region near the middle of the y axis, particles are transported upward over the whole domain. This behavior cannot be explained by the diffusion process because the mixing is not spatially homogeneous. It demonstrates turbulent convection as clouds of sediments are locally ejected with much higher speed than average. The analysis of turbulent flow structures is thus necessary in order to better understand the sediment ejection process. Note that Figure 4 does not indicate that the total vertical flux should be maximum near the flow reversal. As already mentioned, $\bar{w}_p$ is calculated only from particles that do not settle during the experiment. The upward diffusive flux during the maximum flow rates is not properly measured owing to the limitation of number of employed sediment particles. The sediment diffusion is proportional to the gradient of sediment concentration and it may be reduced if the near-bed concentration is low.

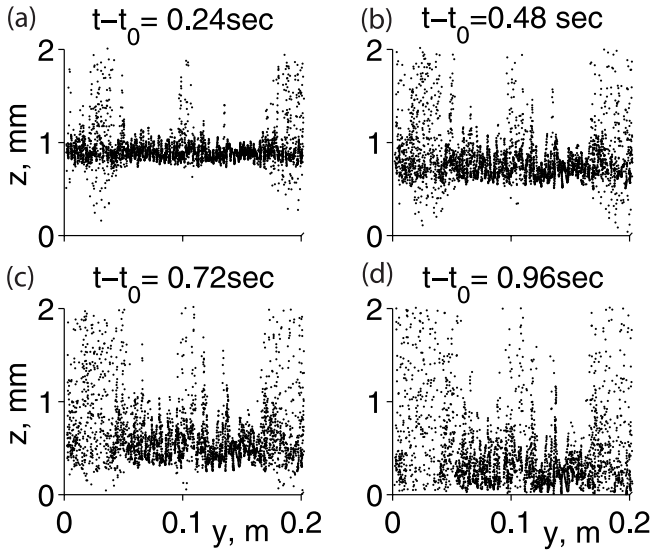

Figure 6. Vertical dispersion of sediment particles on y-z plane at decelerating phase. Particles are released at z = 0.95 mm and $t_0 \sim$ 4.5 s. (a) $t - t_0$ = 0.24 s, (b) $t - t_0$ = 0.48 s, (c) $t - t_0$ = 0.72 s, and (d) $t - t_0$ = 0.96 s.

3.3. Effects of Coherent Structures

[24] In Figure 8 the horizontal distributions of vertical velocity is contoured on a near-bed $x - y$ plane at three times corresponding to the times of particle release in Figures 5–7. During the time of maximum flow (Figure 8a), long streaky lines develop over the plane along the streamwise direction. These streaks are usually pairwise with opposing directions and small velocity magnitudes. Streaks are a well recognized feature of the near-wall region of turbulent boundary layers, being the footprint of streamwise vortices that form at the base of the buffer region [*Robinson*, 1991]. While the dynamics and role of these vortices is reasonably well understood in steady turbulent boundary layers [*Schoppa and Hussain*, 2002], not much is known at present on how they behave under oscillating conditions. In the present case, the period of the flow is sufficiently long [*Scotti and Piomelli*, 2001] that, at least at during maximum flow the streaks should be similar to the ones observed in steady flows, and in fact their spacing (about 100 wall units) is close to what is expected for steady flows. A complete description of the type-dependent behavior of these structures is, however, beyond the scope of this paper. Here we only mention the features that are most likely to affect the transport of sediments.

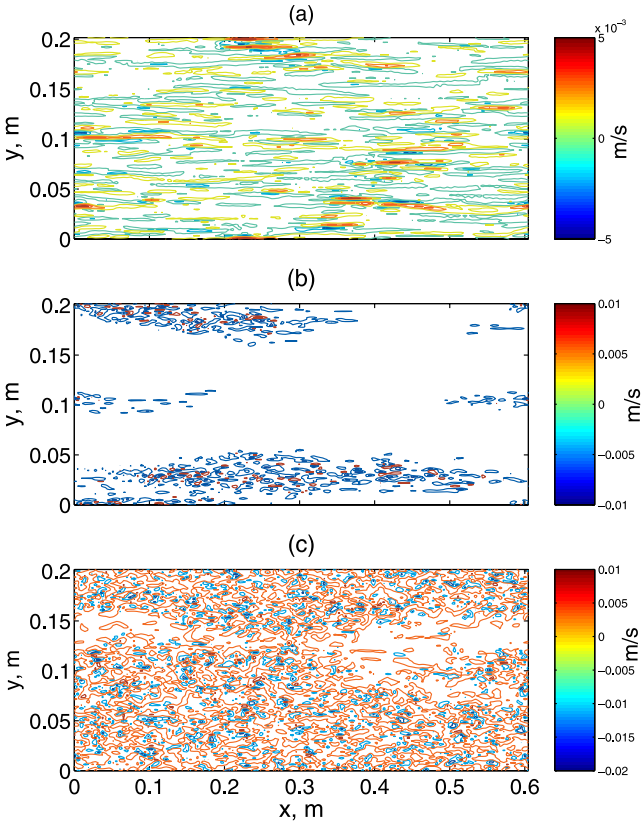

Figure 8. Horizontal distribution of vertical velocity components on x-y plane at z = 1.5 mm (a) at maximum flow rate ($t \sim 4$ s), (b) at deceleration phase ($t \sim 5$ s), and (c) at flow reversal ($t \sim 6.5$ s).

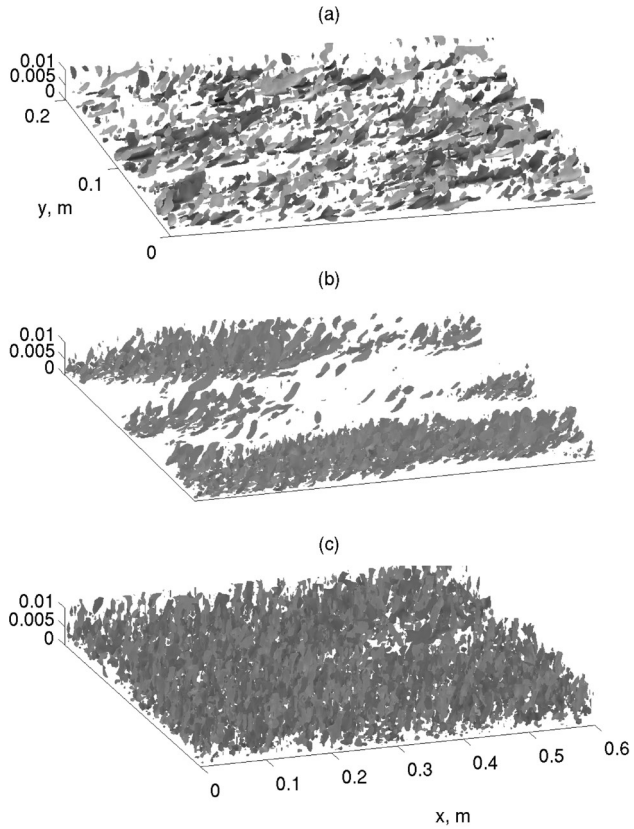

Figure 9. (a) Isosurfaces of $Q = 10$ s^{-2} at maximum flow rate ($t \sim 4$ s), (b) at deceleration phase with $Q = 20$ s^{-2} ($t \sim 5$ s), and (c) at flow reversal with $Q = 50$ s^{-2} ($t \sim 6.5$ s).

[25] During the decelerating phase (Figure 8b), the long streaky structures with small vertical velocities disappear. Instead, spots of strong upward and downward velocities are found close to the spanwise boundaries. The velocity magnitude of these fluctuations is about 1 cm/s, strong enough to move the sediment particles vertically. Near flow reversal (Figures 8c), with the exception of small area at the center, the spots with strong upward and downward velocities are found over the whole domain. If the plots in Figures 8b and 8c are compared with Figures 6 and 7, it is possible to overlap the regions of sediment burstings with the regions of strong vertical velocities. Thus the sediment particles respond to flow structures that develop during the decelerating and reversal flow phases.

[26] These turbulent structures can be visualized through the second invariant Q of the velocity gradient tensor following the approach developed by *Hunt et al.* [1988],

$$Q = -\frac{1}{2}\frac{\partial u_i}{\partial x_j}\frac{\partial u_j}{\partial x_i} = -\frac{1}{2}\left(\| S \|^2 - \| \Omega \|^2\right), \qquad (7)$$

where S and Ω are the symmetric and antisymmetric component of the velocity gradient tensor. During maximum flow (Figure 9a), the coherent structures are aligned in the streamwise direction. In order to examine these streamwise vortices, a representative sample is isolated and magnified in Figure 10a where a pair of vortices are shown aligned in the x direction. Figure 10b shows vorticity contours on a $y - z$ plane with the pair of counter rotating vortices easily recognizable. These are coherent structures that develop in the near-wall region of the turbulent

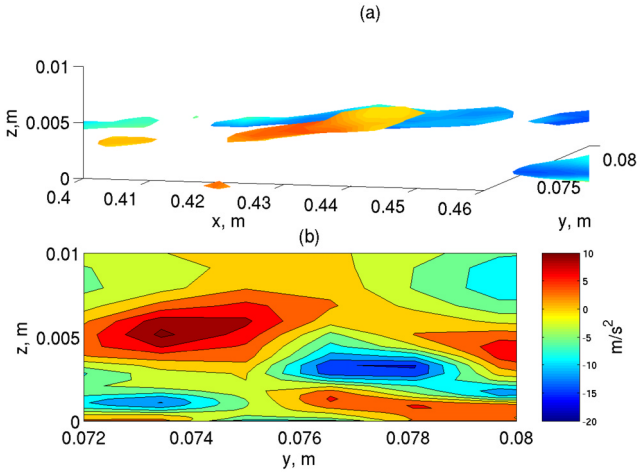

Figure 10. (a) Magnified view of the isosurfaces of $Q = 10$ s^{-2} in Figure 6a at maximum flow rate showing a pair of vortices. (b) Streamwise vorticity contours at a $y - z$ cross section ($x = 0.35$ m). The vortices rotate in the opposite direction.

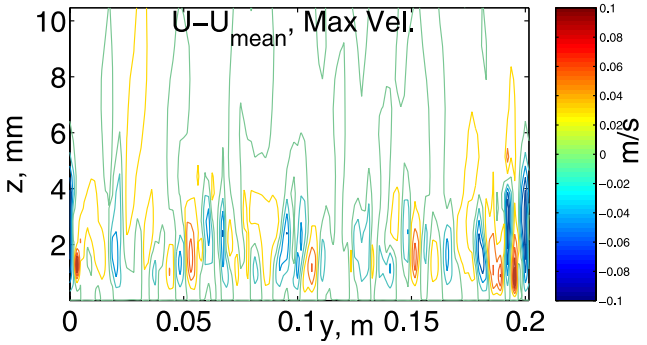

Figure 11. Contours of streamwise flow velocities (demeaned) in a $y - z$ plane at maximum flow rate. Strong coherent structures are found close to the bottom.

boundary layer. It has been found that similar coherent structures were able to capture sediment particles and even transport them over a rippled bed crest [*Chang and Scotti*, 2003]. It is therefore possible that these streamwise coherent structures are also able to keep the sediment particles from settling during the maximum flow phase as observed in Figure 5. In Figure 11 the coherent structures are actively organized near the bottom ($z < 3$ mm), and are strong enough to capture the sediment particles because the maximum magnitude of net streamwise velocities inside the vortices is as big as 10 cm/s. Another example is shown in Figure 12, where the sediment position can be compared to the distribution of coherent structures during maximum flow.

[27] At the onset of the decelerating phase, the topology of coherent structures change (Figure 9b). A group of vertical vortex filaments developed near the spanwise boundaries. overlapping the regions of strong vertical velocities (Figure 8b) and bursting sediments (Figure 6). Clearly these vertical vortices provide a mean for the sediment particles to be ejected with higher dispersion rate than usual. At flow reversal, the vertical vortices are distributed more broadly over the whole domain (Figure 9c). As confirmed in Figure 8c, the magnitude of vertical velocities inside these vortices is maximum at this time resulting in the enhanced sediment ejection (Figures 4 and 7). This active sediment suspension by vertical vortices is due to turbulent convection and is separate from diffusion because of its larger mixing scale. Although it is not easy to quantify this convective flux because of its spatial as well as temporal variation, future work can utilize statistical approaches to test these parameters.

3.4. Effects of Flow Asymmetry

[28] We have examined the effect of flow asymmetry on the suspension rate by considering a pure oscillating flow obtained by setting $\alpha = 0$ in equation (4). In Figure 13 the entrainment rate, $\bar{w_p}$, is compared between the pulsating and pure oscillating cases (Figure 13a) in relation to the flow energy (Figure 13b). The entrainment rate is greatly reduced in the case of pure oscillating flows as the maximum value at the flow reversal is decreased to about 75% although the magnitude differences between the near bed flow velocities are not greater than 20%. The large differences are also found in the turbulent kinetic energy (TKE) distribution. The reduction of the peak values are more than 70%, probably directly related to the reduction in suspension rates. In Figure 14 the vertical velocity distributions of the pure oscillating case are shown in order to facilitate direct comparison with the pulsating flows shown in Figure 8. The velocity magnitudes of vortex cores are greatly reduced in the case of pure oscillating flows at the time of flow reversal although small changes are found at the time of maximum flows. Therefore the asymmetries in unsteady flows may greatly affect the turbulent structures as well as the sediment suspensions during the flow reversal.

4. Discussion and Conclusions

[29] In this paper we investigated the role of coherent structures in the uplifting and dispersal of sediments under

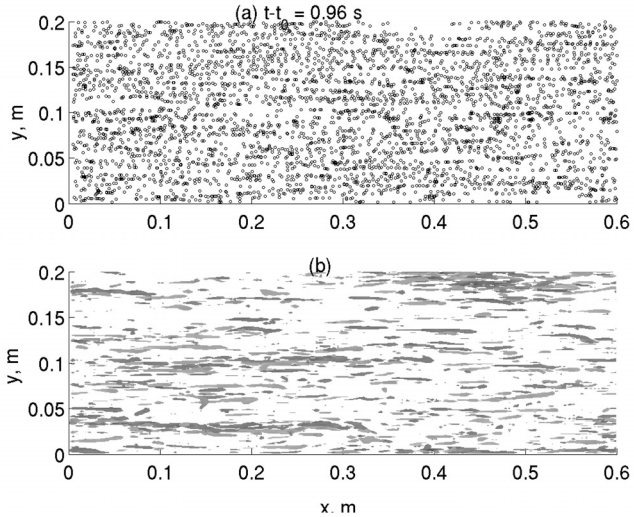

Figure 12. Plane view ($x - y$) of (a) near-bed sediment particle distribution and (b) near-bed turbulent structures at maximum flow rate. Sediments with vertical position between 0.1 and 2.0 mm are shown.

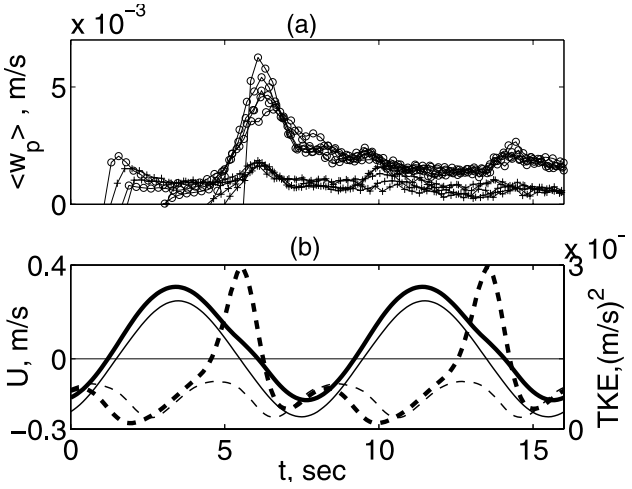

Figure 13. (a) Vertical components of mean particle velocity: circles, pulsating flow; crosses, pure oscillation flow. (b) Near-bed streamwise velocity (solid line) and turbulent kinetic energy (dashed line): thick lines, pulsating flow; thin lines, pure oscillating flow.

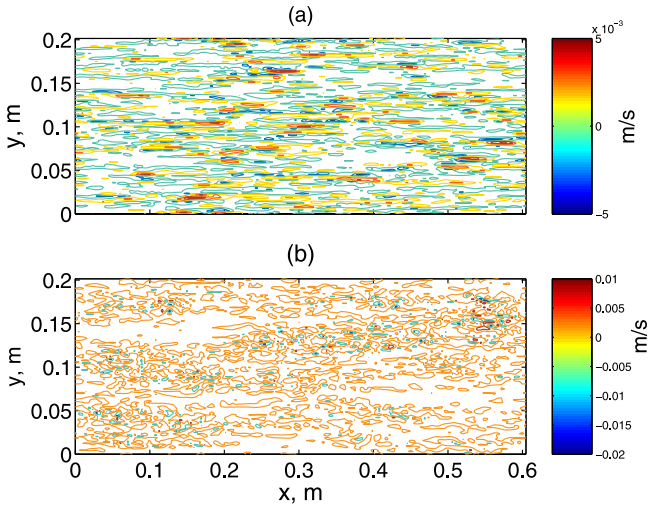

Figure 14. Horizontal distribution of the vertical velocity components for pure oscillating flow ($\alpha = 0$) (a) at maximum flow rate and (b) at flow reversal.

pulsating conditions. During times of maximum flow the vortex cores are parallel to the streamwise direction. The resulting flow is able to maintain sediments suspended, but no significant uplifting is observed. At the onset of flow deceleration, vertically developed vortices cause the sediment to be ejected. This sediment ejection mechanism is only active near the bed because the development of these vortices is confined within a thin layer close to bottom. This is illustrated in Figure 13, where the peak of entrainment rate has been reduced in one wave cycle owing to the majority of sediment particles being suspended and located far from the vertical vortex effects.

[30] This active sediment convection due to vertical turbulent vortices requires the a modification of standard models for sediment suspension. Most of the Reynolds-Averaged models (RANS) include the effect of turbulent mixing by means of an eddy diffusivity, that is the vertical sediment flux q in these models is expressed as

$$q = (W - w_s)C + \nu_t \frac{\partial C}{\partial z}. \tag{8}$$

[31] Over a flat bed, the mean velocity W is zero, and the eddy diffusivity, ν_t, is a function of time only, so the total flux should remain homogeneous. The spatially variable rates of sediment suspension found during the flow deceleration and reversal times are not supported by equation (8). We emphasize that this conclusion applies only to eddy-diffusivity models, in which the flux is assumed to be proportional to the gradient. More complex models, based on PDF approach or higher-order equations for the Reynolds correlations (e.g., $\langle w'c' \rangle$) might not suffer the limitations of the simpler, gradient-based diffusion models.

[32] In order to include the convective flux, *Nielsen* [1992] suggested a conceptual model in which the convection is contributed by a pick-up function, $p(t)$, and a probability function of sediment entrainment level, $F(z)$,

$$q' = (W - w_s)C + \nu_t \frac{\partial C}{\partial z} + p(t)F(z). \tag{9}$$

Lee and Hanes [1996] showed that the mean profiles of suspended sediments based on equation (9) were better supported by measurements than the models based on diffusion or convection alone. However, it is still necessary to test the convection term quantitatively because the probability function was arbitrary and not based upon experimental results. In addition, the pick-up function should be tested under unsteady conditions because the original formula by *van Rijn* [1984a] was set up in steady flows.

[33] Perhaps one of the most important tasks in modeling the convective flux is to determine the timing of maximum sediment ejection. *Vittori* [2003] reported maximum suspension rates during the decelerating flow phase. Here we find that a better predictor for ejection is the local time of flow reversal. We also found differences between pulsating and oscillating flows. The effect of flow reversal is large in pulsating flow while it is significantly reduced in the pure oscillating flow and so active sediment ejection during flow reversal may be weaker in purely oscillating flows.

[34] **Acknowledgments.** We thank E. Balaras for providing the serial Navier-Stokes solver that forms the basis of the code employed in this work. We also thank the UNC-CH ITS Research Computing group for computer time and support. Research supported by NSF grants OCE-0351667 and OCE-9910883.

References

Andersen, K. H. (1999), The dynamics of ripples beneath surface waves, Ph.D. thesis, Tech. Univ. of Denmark, Lyngby, Denmark.

Armenio, V., U. Piomelli, and V. Fiorotto (1999), Effect of the subgrid scales on particle motion, *Phys. Fluids*, *11*, 3030–3042.

Bagnold, R. (1954), The flow of cohesionless grains in fluids, *Philos. Trans. R. Soc.*, *249*, 235.

Balachandar, S., and M. R. Maxey (1989), Methods for evaluation of velocities in spectral simulations of turbulence, *J. Comput. Phys.*, *83*, 96–125.

Balaras, E. (1995), Finite difference computations of high Reynolds-number flows using the dynamic subgrid-scale model, *Theor. Comput. Fluid Dyn.*, *7*(3), 207–216.

Chang, Y., and D. Hanes (2004), Suspended sediment and hydrodynamics above mildly sloped long wave ripples, *J. Geophys. Res.*, *109*, C07022, doi:10.1029/2003JC001900.

Chang, Y., and A. Scotti (2003), A numerical study of entrainment and suspension of sediments into a turbulent flow over ripples, *J. Turb.*, *4*(19), 1–22.

Chang, Y., and A. Scotti (2004), Modeling unsteady turbulent flows over ripples: Reynolds-averaged Navier-Stokes equations (RANS) versus large-eddy simulation (LES), *J. Geophys. Res.*, *109*, C09012, doi:10.1029/2003JC002208.

Drake, T. G., and J. Calantoni (2001), Discrete particle model for sheet flow sediment transport in the nearshore, *J. Geophys. Res.*, *106*(C9), 19,859–19,868.

Einstein, H. A. (1950), The bed load function for sediment transportation in open channels, *Tech. Bull. 1026*, Soil Conserv. Serv., U.S. Dep. of Agric., Washington, D. C.

Eungelund, F., and J. Fredsoe (1976), A sediment transport model for straight alluvial channels, *Nord. Hydrol.*, *7*(5), 293–306.

Fredsoe, J., and R. Deigaard (1992), *Mechanics of Coastal Sediment Transport*, vol. 3, p. 203, World Sci., Hackensack, N. J.

Garcia, M., and G. Parker (1991), Entrainment of bed sediment into suspension, *J. Hydraul. Eng.*, *117*(4), 414–435.

Germano, M., U. Piomelli, P. Moin, and W. Cabot (1991), A dynamic subgrid-scale eddy viscosity model, *Phys. Fluids A*, *3*, 1760–1765.

Hino, M., M. Kashiwayanagi, A. Nakayama, and T. Hara (1983), Experiments on the turbulent statistics and the structure of a reciprocating oscillatory flow, *J. Fluid Mech.*, *131*, 363–400.

Holmedal, L., D. Myrhaug, and K. Eidsvik (2004), Sediment suspension under sheet flow conditions beneath random waves plus currents, *Cont. Shelf Res.*, *24*, 2065–2091.

Hunt, J. C. R., A. A. Wray, and P. Moin (1988), Eddies, streams and convergence zones in turbulent flows, in *CTR Annual Research Briefs*, p. 193, NASA Ames/Stanford Univ., Stanford, Calif.

Kim, J., P. Moin, and R. Moser (1987), Turbulence statistics in fully developed channel flow at low reynolds number, *J. Fluid Mech.*, *177*, 133–166.

Launder, B., and B. Sharma (1974), Application of the energy dissipation model of turbulence to the calculation of flow near a spinning disc, *Lett. Heat Mass Transfer*, *1*, 131–138.

Lee, T., and D. Hanes (1996), Comparison of field observations of the vertical distribution of suspended sand and its prediction by models, *J. Geophys. Res.*, *101*(C2), 3561–3572.

Li, Z., and A. Davis (1996), Towards predicting sediment transport in combined wave-current flow, *J. Waterw. Port Coasal Ocean Eng.*, *122*(4), 157–164.

Lilly, D. (1992), A proposed modification of the Germano subgrid-scale closure method, *Phys. Fluids A*, *4*, 633–634.

Marchioli, C., V. Armenio, M. V. Salvetti, and A. Soldati (2006), Mechanism for deposition and resuspension of heavy particles in turbulent flow over wavy interfaces, *Phys. Fluid*, *18*, doi:10.1063/1.2166453.

Maxey, M., and J. Riley (1983), Equation of motion for a small rigid sphere in a non-uniform flow, *Phys. Fluids*, *26*, 883–889.

Moin, P., and J. Kim (1982), Numerical investigation of turbulent channel flow, *J. Fluid Mech.*, *118*, 341–377.

Moin, P., and K. Manesh (1998), Direct numerical simulation: A tool in turbulence research, *Annu. Rev. Fluid Mech.*, *30*, 539–578.

Nielsen, P. (1992), *Coastal Bottom Boundary Layers and Sediment Transport*, vol. 4, World Sci., Hackensack, N. J.

O'Donoghue, T., and S. Wright (2004), Concentrations in oscillatory sheet flow for well sorted and graded sands, *Coastal Eng.*, *50*, 117–138.

Patankar, N., T. Ko, H. Choi, and D. Joseph (2001), A correlation for the lift-off of many particles in plane poiseuille flows of newtonian fluids, *J. Fluid Mech.*, *445*, 55–76.

Pedinotti, S., G. Mariotti, and S. Banerjee (1992), Direct numerical simulation of particle behavior in the wall region of turbulent flows in horizontal channels, *Int. J. Multiphase Flow*, *18*(6), 927–941.

Robinson, S. K. (1991), Coherent motions in the turbulent boundary layer, *Annu. Rev. Fluid Mech.*, *23*, 601–639.

Rogallo, R., and P. Moin (1984), Numerical simulation of turbulent flows, *Annu. Rev. Fluid Mech.*, *16*, 99–137.

Saffman, P. (1970), A model for inhomogeneous turbulent flow, *Proc. R. Soc. Ser. A*, *317*, 417–433.

Scandura, G., G. Vittori, and P. Blondeaux (2000), Three-dimensional oscillatory flow over steep ripples, *J. Fluid Mech.*, *412*, 355–378.

Schoppa, W., and F. Hussain (2002), Coherent structure generation in near-wall turbulence, *J. Fluid Mech.*, *453*, 57–108.

Scotti, A., and U. Piomelli (2001), Numerical simulation of pulsating turbulent channel flow, *Phys. Fluids*, *13*, 1367–1384.

Smith, J., and S. McLean (1977), Spatially averaged flow over a wavy surface, *J. Geophys. Res.*, *82*(12), 1735–1746.

Tjerry, S. (1995), Morphological calculations of dunes in alluvial rivers, Ph.D. thesis, Tech. Univ. of Denmark, Lyngby, Denmark.

van Rijn, L. C. (1984a), Sediment pickup functions, *J. Hydraul. Eng.*, *110*(10), 1494–1502.

van Rijn, L. C. (1984b), Sediment transport: Part II. Suspended load transport, *J. Hydraul. Eng.*, *110*(11), 1613–1641.

van Rijn, L. C. (1986), Applications of sediment pick-up function, *J. Hydraul. Eng.*, *112*(9), 867–875.

Vittori, G. (2003), Sediment suspension due to waves, *J. Geophys. Res.*, *108*(C6), 3173, doi:10.1029/2002JC001378.

Vittori, G., and R. Verzicco (1998), Direct simulation of transition in an oscillatory boundary layer, *J. Fluid Mech.*, *371*, 207–232.

Wang, Q., and K. Squires (1996), Large eddy simulation of particle-laden turbulent channel flow, *Phys. Fluids*, *8*, 1207–1223.

Wiberg, P., and J. Smith (1985), A theoretical model for saltating grains in water, *J. Geophys. Res.*, *90*(C4), 7341–7354.

Wilcox, D. C. (1998), *Turbulence Modeling for CFD*, DCW Ind., Inc., La Cañada, Calif.

Zedler, E., and R. Street (2001), Large-eddy simulation of sediment transport: current over ripples, *J. Hydraul. Eng.*, *127*(6), 444–452.

Zyserman, J., and J. Fredsoe (1994), Data analysis of bed concentration of suspended sediment, *J. Hydraul. Engrg.*, *120*(9), 1021–1042.

Y. S. Chang, Meteorology and Physical Oceanography, Rosenstiel School of Marine and Atmospheric Science, University of Miami, Miami, FL 33149, USA. (ychang@rsmas.miami.edu)

A. Scotti, Department of Marine Sciences, University of North Carolina, Chapel Hill, NC 27599, USA. (ascotti@unc.edu)